The Astrophysical Journal, 969:22 (11pp), 2024 July 1 https://doi.org/10.3847/1538-4357/ad429a

Radio Images inside Highly Magnetized Jet Funnels Based on Semianalytic GRMHD Models

Taiki Ogihara[1], Tomohisa Kawashima[2], and Ken Ohsuga[1]
[1] Center for Computational Sciences, University of Tsukuba, Ten-nodai, 1-1-1 Tsukuba, Ibaraki 305-8577, Japan; taiki.ogihara@gmail.com
[2] Institute for Cosmic Ray Research, The University of Tokyo, 5-1-5 Kashiwanoha, Kashiwa, Chiba 277-8582, Japan

Received 2023 October 15; revised 2024 April 19; accepted 2024 April 22; published 2024 June 25

Abstract

By performing general-relativistic radiative transfer calculations, we show the radio images of relativistic jets including highly magnetized regions inside jet funnels, based on steady, axisymmetric, and semianalytic general-relativistic magnetohydrodynamics models. It is found that multiple ring images appear at the photon frequency of 230 GHz for nearly pole-on observers, because of the strong light-bending effect on photons generated at the separation surface, which is the boundary between the inflow and outflow flows in the jet funnel. A bright teardrop-shaped component, which extends from the bright rings of the separation surface, also appears in the counterjet region. The diameter of the brightest outermost ring originated from the counterjet is ∼60 μas, which is consistent with the ringlike images of M87 at 86 GHz observed with GMVA, the Atacama Large Millimeter/submillimeter Array, and the Greenland Telescope, whose ring diameter is $\sim 64^{+4}_{-8}$ μas. The thinner and smaller-diameter rings are exhibited when the black hole spin magnitude is higher. These morphological features are expected to appear without being prominently affected by the detailed magnetohydrodynamic plasma parameters of our general-relativistic ideal magnetohydrodynamic (GRMHD) jet model, since the location of the separation surface is mainly regulated by the black hole spin. Our GRMHD model and the emission features of the images in the horizon-scale, highly magnetized jet funnel may be tested by future observations, e.g., the next-generation Event Horizon Telescope and the Black Hole Explorer.

Unified Astronomy Thesaurus concepts: Active galactic nuclei (16); Black hole physics (159); General relativity (641); Relativistic jets (1390); Magnetohydrodynamics (1964)

1. Introduction

Relativistic jets have been observed in active galactic nuclei (AGNs). High-resolution very-long-baseline interferometry (VLBI) radio observations have resolved the detailed emission structures of AGN jets. Limb-brightened structures have been observed at millimeter–centimeter wavelengths in jets of M87 (Kovalev et al. 2007; Walker et al. 2008, 2018; Hada et al. 2011, 2016; Mertens et al. 2016; Kim et al. 2018), Mrk 501 (Piner et al. 2009), Mrk 421 (Piner et al. 2010), Cyg A (Boccardi et al. 2016), 3C 84 (Nagai et al. 2014; Giovannini et al. 2018), Cen A (Janssen et al. 2021), 3C273 (Bruni et al. 2021), PKS 1749 + 096 (Cui et al. 2021), NGC 315 (Park et al. 2021), and PG 1553 + 113 (Orienti et al. 2020). A triple-ridge structure composed of the limb-brightened components and an additional central bright component has been observed in the M87 jet (Asada et al. 2016; Hada et al. 2017; Walker et al. 2018). The jet width profiles along the distance from the black hole (BH) have been measured in several jets (Asada & Nakamura 2012; Boccardi et al. 2016, 2021; Tseng et al. 2016; Hada et al. 2018; Nakamura et al. 2018; Nakahara et al. 2019, 2020; Kovalev et al. 2020; Park et al. 2021; Cui et al. 2023; Lu et al. 2023).

It is crucial to reveal the formation mechanism of relativistic jets via studies of the jet-launching region. AGN jets are thought to be launched near a central supermassive BH. The Event Horizon Telescope (EHT) has revealed the ringlike emission structure around the event horizon of M87 at 230 GHz (Event Horizon Telescope Collaboration 2019a, 2019b, 2019c, 2019d, 2019e, 2019f). However, an extended emission structure that connects to the jet seen in the lower-frequency observations has not been confirmed. Future high-resolution observations are expected to reveal the extended images from the jet at its launching zone (Doeleman et al. 2019).

The formation mechanism of the jets near a central supermassive BH is still under debate. One of the plausible jet-launching mechanisms is the Blandford–Znajek process (Blandford & Znajek 1977). The BH spin twists the magnetic field lines threading the BH, generates the Poynting flux extracting the rotation energy from the BH, and accelerates the plasma to relativistic speed. The dynamics of AGN jets have been studied both analytically and numerically.

Numerical general-relativistic ideal magnetohydrodynamic (GRMHD) simulations have been performed to investigate the surroundings of a BH (Koide et al. 1998; De Villiers et al. 2003; McKinney & Gammie 2004; Mizuno et al. 2006; White et al. 2016; Porth et al. 2019; see also Mizuno 2022 for a review). Highly magnetized funnel regions, which are also indicated by analytical works on the observation data (Kino et al. 2014, 2015), are formed along the spin axis of the rotating BH, and the relativistically accelerated jets appear there. However, such simulations have numerical difficulties in exactly calculating the highly magnetized jet regions, because of the significant contaminations due to artificial floors on the density and internal energy. Some simulations also have artificial ceilings on the magnetization parameter, the ratio of the electromagnetic energy flux to the rest-mass energy flux.

Because of the problem mentioned above, a number of general-relativistic radiative transfer (GRRT) calculations have been carried out neglecting the emission and absorption in the highly magnetized jet regions in the GRMHD simulation data, in order to avoid the artificial and uncertain appearance of the relativistic jets (e.g., Dexter et al. 2009, 2012; Mościbrodzka et al. 2014, 2016; Gold et al. 2017; Davelaar et al. 2019; Tsunetoe et al. 2020; Kawashima et al. 2023). In practice, O'Riordan et al. (2018) showed significant observational differences in the synthetic spectra, particularly in the optical and X-ray bands, between the models in which the funnel is empty and the models where the funnel is filled with plasma, and Chael et al. (2019) demonstrated synthetic images and spectra with different ceiling values of magnetization parameters. These studies showed that the floor or ceiling values bring uncertainty to synthetic images, while this effect is not significant when the magnetization is not so high in the highly magnetized region (Chael et al. 2019; Event Horizon Telescope Collaboration et al. 2021).

Alternative to the GRMHD simulation studies, analytical works have been carried out. While it is somewhat difficult to incorporate the time-dependent dynamics, it is possible to study the highly magnetized region of the relativistic jets. For example, force-free jets have been studied (e.g., Zakamska et al. 2008; Broderick & Loeb 2009; Gracia et al. 2009) and the improved models of Takahashi et al. (2018) and Ogihara et al. (2019) have reproduced the observed jet structures in jets, e.g., the limb-bright structure and triple-ridge structure, respectively.

While the force-free approximation is appropriate for the extremely magnetized region, it is difficult to study the jets with their non-negligible internal and/or kinetic energy. Analytical GRMHD approaches have therefore also been developed to overcome this problem. The basic equations are divided into parallel and perpendicular components to the magnetic field line. The parallel component is analytically solvable under the assumption of the magnetic flux function and four integral constants (Bekenstein & Oron 1978; Camenzind 1986a, 1986b; Takahashi et al. 1990; Pu et al. 2015; Pu & Takahashi 2020; Ogihara et al. 2021). The perpendicular component has analytic solutions in the force-free limit for the low-BH spin case. They are called the monopole and parabolic Blandford & Znajek perturbation solution (Blandford 1976; Blandford & Znajek 1977). For higher-BH spin cases, Tanabe & Nagataki (2008) derived higher-order terms of the perturbation solutions, and they confirmed the analytically derived total energy flux is consistent with the numerical results in the monopole field-line case. Nathanail & Contopoulos (2014) conducted numerical force-free simulations, and they showed the field-line configurations inside the fixed monopole and parabolic field lines.

In the steady and axisymmetric GRMHD formulation, Huang et al. (2019) and Huang et al. (2020) studied two-dimensional distributions of the electromagnetic field, the density, and the velocity of plasma by iteratively solving the parallel component and the perpendicular component for the monopole and parabolic field-line configuration. In the parabolic field-line model, they introduced the "loading zone." The inner boundary of the loading zone is the null-charge surface, and the outer boundary is the surface where the outflow velocity obtained by solving the Bernoulli equation becomes zero. The outflow and inflow start at these surfaces. Ogihara et al. (2021) constructed two-dimensional jet models without the loading zone by solving the Bernoulli equation analytically and the trans-field force balance numerically only at the separation surface of the inflow and the outflow. The force balance is relatively well established near the separation surface and far from the BH. It will be fruitful to demonstrate the appearance of the highly magnetized jets inside the jet funnels in future VLBI missions with high resolution and high sensitivity, to detect the images of horizon-scale jets.

In this paper, we compute synthetic radio images of highly magnetized relativistic jets inside the jet funnels based on the semianalytic GRMHD models of Ogihara et al. (2021). We focus on the emission structure of the jets in the vicinity of the BH horizon, which is thought to be the origin of the jet. As a first attempt, we demonstrate the observational features of highly magnetized jets based on the semianalytic GRMHD model, rather than focusing on tuning the model parameters reproducing the observed image precisely.

This paper is organized as follows. In Section 2, we briefly introduce the GRMHD jet models and the GRRT code we use. In Section 3, we show the resultant synthetic images and their characteristic features. In Section 4, we discuss comparisons to the observed images and other studies. Summary and prospects are presented in Section 4.

2. Method

To compute synthetic images of the semianalytic GRMHD models of Ogihara et al. (2021), we perform the GRRT calculations using the `RAIKOU` code (Kawashima et al. 2023). Here, we focus on the emission features of relativistic jets, treating the outside of the jets as a vacuum.

The spacetime geometry is given by the Kerr metric in the Boyer–Lindquist coordinates,

$$ds^2 = -\left(1 - \frac{2Mr}{\Sigma}\right)c^2dt^2 - \frac{4aMr\sin^2\theta}{\Sigma}dtd\phi + \frac{\Sigma}{\Delta}dr^2 + \Sigma d\theta^2 + \frac{[(r^2+a^2)^2 - \Delta a^2\sin^2\theta]\sin^2\theta}{\Sigma}d\phi^2, \tag{1}$$

where $\Sigma = r^2 + a^2M^2\cos^2\theta$, $\Delta = r^2 - 2Mr + a^2M^2$. M is the BH mass. The gravitational radius is $r_{\rm g} = GM/c^2$. a, c, and G are the dimensionless spin parameter, speed of light, and gravitational constant, respectively. In Equation (1), we set $c = G = 1$. The radius of the event horizon is $r_{\rm H} = r_{\rm g}(1 + \sqrt{1-a^2})$. The angular velocity of the BH is $\Omega_{\rm H} = ac/2r_{\rm H}$.

2.1. GRMHD Jet Model

Ogihara et al. (2021) constructed steady, axisymmetric GRMHD jet models. They assumed fixed poloidal magnetic field shapes that mimic force-free analytic solutions and GRMHD simulation results. The field-line shapes are defined by the flux function

$$\Psi(r, \theta) = C\left[\left(\frac{r}{r_{\rm H}}\right)^{\nu}(1-\cos\theta) + \frac{1}{4}\epsilon\frac{r}{r_{\rm g}}\sin\theta\right], \tag{2}$$

where C is the normalization factor that sets the magnetic field strength as 10 G at the ergosphere of the outermost field line. They only consider the field line threading the BH. ν and ϵ are the model parameters controlling the poloidal field-line shape. When $\epsilon = 0$, the field-line configurations of $\nu = 0$ and $\nu = 1$

have the monopole and parabolic shape in the far zone, respectively.

There are four integral constants along the field line: the total energy flux per particle E, the total angular momentum flux per particle L, the number density flux per magnetic flux η, and the so-called "angular velocity of the magnetic field" Ω_{F} (Bekenstein & Oron 1978). Ogihara et al. (2021) determined the value of these integral constants by four conditions: the regularity condition at the fast magnetosonic point in the outflow, the Znajek condition (Znajek 1977), the initial poloidal velocity at the separation surface, and the force balance at the separation surface. The separation surface is given by the surface where $\partial_p k_0 = 0$ for each field line, where ∂_p is the directive differentiation along the field line and $k_0 = -(g_{00} + 2\Omega_{\mathrm{F}} g_{03} + \Omega_{\mathrm{F}}^2 g_{33})$. There are five free parameters in the models in Ogihara et al. (2021), which are the BH's dimensionless spin parameter a, the field-line configurations ν and ϵ, the poloidal four velocity at the separation surface, and the angular velocity of the outermost field line threading the BH.

In this paper, we use the jet models P1, P2, and P3 of Ogihara et al. (2021). The P1 model is the fiducial one, in which the BH spin parameter is $a = 0.9$. The P2 and P3 models have $a = 0.8$ and 0.95, respectively. $\nu = 1$ and $\epsilon = 10^{-4}$ for all the models. The poloidal four velocity at the separation surface ($r = r_{\mathrm{ss}}$) is given by $u_p(r = r_{\mathrm{ss}}) = 10^{-3}$. The angular velocity of the outermost field line threading the BH is given by $\Omega_F(\Psi = \Psi_{\max}) = 0.35\Omega_{\mathrm{H}}$, where $\Psi_{\max}$ is the value of the flux function at the outermost field line. The force balances between the field lines are numerically solved only at the separation surface from $\Psi = \Psi_{\max}$ toward the jet axis. As a consequence, the distributions of the toroidal magnetic field, poloidal electric field, matter velocity, and density on each field line are analytically obtained. The other model parameters are the same among the models. Notable differences between the models are as follows: (i) the maximum value of the magnetization parameter is higher in the model with a larger spin, and (ii) the density at the separation surface is higher at the jet edge and lower near the jet axis when the spin is larger (see Figure 4 in Ogihara et al. 2021). We use the data of the GRMHD models from the radius of the ergosphere to $\sim 10^5 r_{\mathrm{g}}$. We do not consider the emission from the outside of the jet boundary $\Psi = \Psi_{\max}$ and inside the ergosphere. Near the jet axis, in the white region in Figure 3, the electromagnetic field, velocity field, and density are filled with the values from the closest cell.

2.2. GRRT Calculation

The nonthermal synchrotron radio images of the GRMHD jet models are computed by using a general-relativistic multiwavelength radiative transfer code `RAIKOU` (Kawashima et al. 2023). In the `RAIKOU` code, two types of algorithms are implemented: (i) the observer-to-emitter ray-tracing algorithm for efficient calculations of the non-Compton-scattered photons; and (ii) the emitter-to-observer Monte Carlo algorithms for the broadband multiwavelength calculations including Compton processes. In this work, we employ the observer-to-emitter ray-tracing algorithm for efficient calculations of the synchrotron radio images of the jets.

In this paper, we use the parameter values dedicated to M87. We set the BH mass and the distance to the BH to be $6.5 \times 10^9 M_{\odot}$ and 16.9 Mpc (Event Horizon Telescope Collaboration 2019f), respectively. In our fiducial model, the viewing angle from the jet axis is $\theta_{\mathrm{view}} = 15°$. In addition, we also examine $\theta_{\mathrm{view}} = 5°$, 45°, and 85° to generally understand the observational signature of our jet model via the comparison among them.

We assume that all the particles consist of single-power-law nonthermal electrons and we consider the synchrotron emission and absorption from them. We mainly study the models with the steeper power-law index $p = -3.5$ (e.g., Dexter et al. 2012; Kawashima et al. 2021), where $N(\Gamma_{\mathrm{e}}) \propto \Gamma_{\mathrm{e}}^p$. N is the particle number density in the phase space and Γ_{e} is the electron's Lorentz factor. We also discuss the dependence of the jet's appearance on the power-law index through the comparison with the model with the shallower power-law index $p = -1.1$. For all models, the minimum and maximum values of Γ_{e} are 30 and 10^6, respectively, which are the same as Kawashima et al. (2021).

In our GRMHD jet model, the magnetic field strength is set in such a way that the field strength at the outer boundary of the ergosphere on the equatorial plane is $B = 10$ G, as is described in Section 2.1. The nonthermal electron density is converted to cgs units by multiplying the square of the normalization factor of the magnetic field strength.

3. Results

We first present the results of the GRRT calculation for the fiducial model, in which $a = 0.9$, $\theta_{\mathrm{view}} = 15°$, $p = -3.5$, and the observational frequency is 230 GHz. The emission sources that contribute to the observed images are shown. Then we also show the dependence of the synthetic images on the viewing angle, observational frequency, BH spin, and the power-law index of the electrons. Again, it would be worth mentioning here that the scope of this paper is demonstrating the appearance of the radio image of the highly magnetized, semianalytic GRMHD jet model of Ogihara et al. (2021). The detailed model parameters are not tuned for reproducing the observed radiative fluxes at ∼0.5 Jy, both at 230 GHz by EHT (Event Horizon Telescope Collaboration 2019a) and at 86 GHz by GMVA, the Atacama Large Millimeter/submillimeter Array (ALMA), and the Greenland Telescope (GLT; Lu et al. 2023) in M87, but the magnetic field strength of the outermost field line of the jet at the equatorial plane is fixed to 10 G, as mentioned in Section 2. In our fiducial model, the resulting radiative fluxes are ∼2 and ∼1.8 Jy at 230 and 86 GHz, respectively.

3.1. Synthetic Images

Figure 1 shows the intensity and the optical depth maps of the fiducial model. In each panel, the zero-angular-momentum photons pass through the origin of the observer screen (X, Y) = (0, 0), i.e., the center of the BH is projected to the origin of the screen. The projected length of r_{g} is $\arctan(r_{\mathrm{g}}/D) \sim 3.8\,\mu as$ on the screen. The deprojected length of r_{g} in the direction of the BH spin axis, i.e., the jet direction, corresponds to $\arctan(r_{\mathrm{g}} \sin(\theta_{\mathrm{view}})/D) \sim 0.98\mu as$ in the Y-direction on the screen, when the viewing angle is $\theta_{\mathrm{view}} = 15°$. The log-scale intensity map (left panel) is composed of four bright rings, a bright teardrop-shaped component extending downward from the bright rings, and the broadly extended component that outlines the entire jet shape.

We label the four rings as rings (a), (b), (c), and (d), from the smallest to the largest. The rings (a) and (b) are due to radiation from the bottom of the separation surface in the approaching jet. Meanwhile, the emission from the bottom of the separation

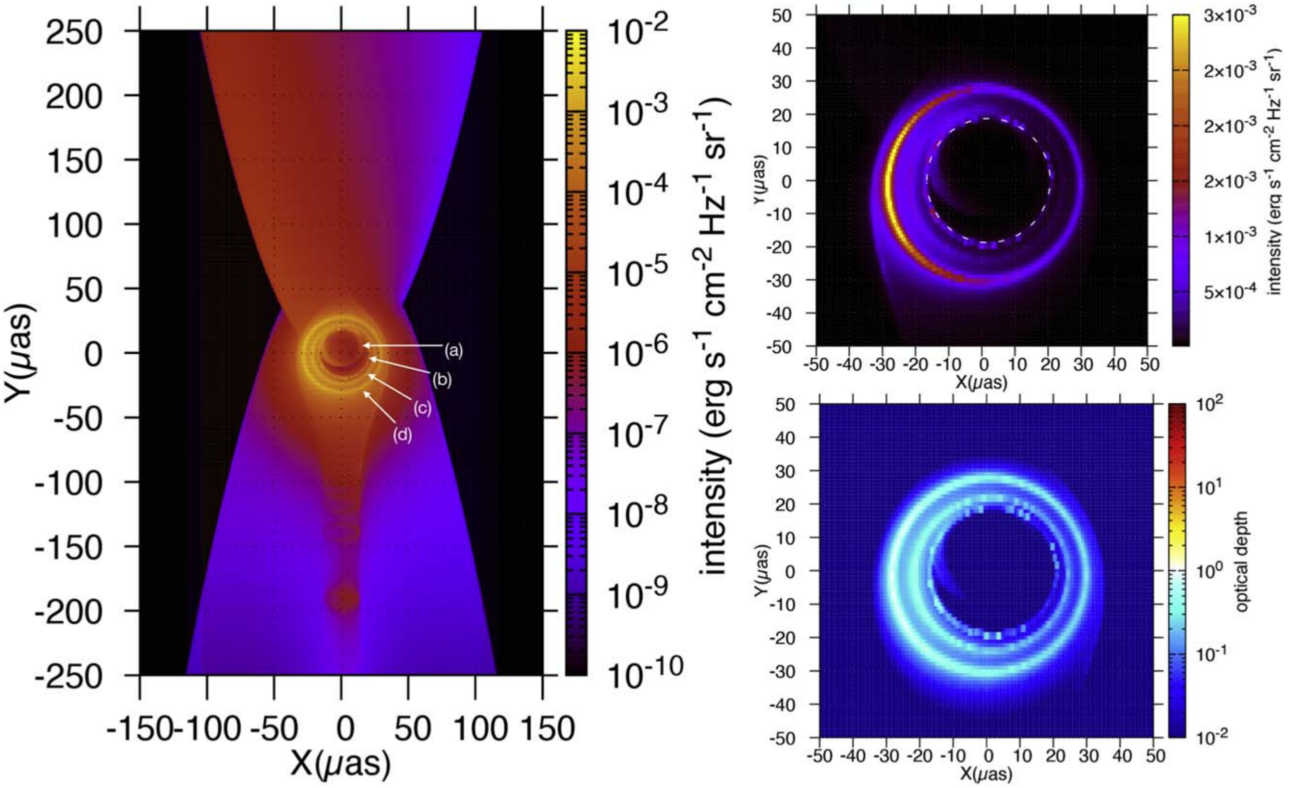

Figure 1. The synthetic images on logarithmic (left panel) and linear scales (right upper panel) with the fiducial parameter set, i.e., BH spin parameter $a = 0.9$, viewing angle $\theta_{\rm view} = 15°$, power-law index $p = -3.5$, and the observational frequency 230 GHz. The optical depth map is plotted in the lower right panel. The white dashed circle in the upper right panel represents the position of the photon ring. The several thin, ringlike red discontinuities seen in the teardrop shape in the counterjet between around $Y \sim -100$ and -200μas are the artifacts resulting from the limited resolution of the semianalytic model used to generate this image and have no physical meaning.

surface in the counterjet produces rings (c) and (d). The emission from near the separation surface contributes to the formation of the teardrop-shaped bright region in the counterjet. We will discuss the details later.

The relativistic beaming is the cause of the asymmetry in the broadly extended regions. The approaching jet is brighter than the counterjet because the approaching jet (counterjet) is moving toward (away from) the observer, except in the inflow regions on the BH side of the separation surface. The asymmetry of the broadly extended regions with respect to the Y-axis is due to the relativistic beaming effect by the toroidal component of the fluid velocity.

The upper right panel of Figure 1 is the linear-scale intensity map cropped by $100 \times 100\,\mu$as from the log-scale intensity map. The white dashed circle indicates the position of the photon ring. Of the two clearly visible rings, the inner one is ring (c) and the outer one is ring (d). The rings (a) and (b) are too dark to see clearly in this panel. The diameter of the outermost brightest ring (d) is $\sim 60\,\mu$as, which is ~ 1.5 times larger than that of the ringlike image observed by EHT and similar to that observed by GMVA (Lu et al. 2023). The possible application of our model and the consistency with the observations will be discussed in Sections 3.3.2 and 4.

In the lower right panel of Figure 1, the optical depth map is demonstrated. The optical depth becomes nearly unity at the bright rings, although the other area is optically thin. This indicates that the ray forming the bright rings passes through the high-opacity (i.e., high-emissivity) regions, with the larger path length due to the light-bending effects.

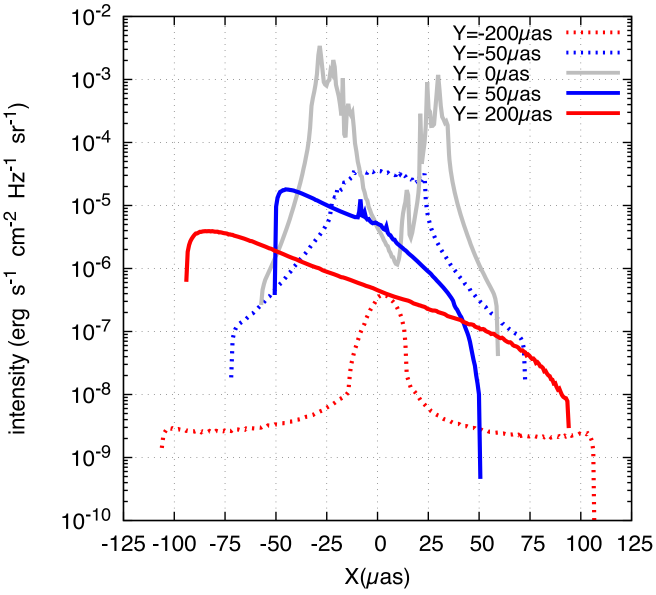

Figure 2. The intensity slices at $Y = -200$, -50, 0, 50, and 200 μas of Figure 1.

In order to quantitatively understand the distribution of the intensity, we show the intensity slices at $Y = -200$, -50, 0, 50, and 200μas in Figure 2. The positions of two intensity peaks, $X \sim \pm 25\mu$as for the slice at $Y = 0$ (gray line), correspond to the four rings. In the slices at $Y = -50\mu$as (blue dotted) and $Y = -200\mu$as (red dotted), the bright parts in

$-25\mu\mathrm{as} \lesssim X \lesssim 25\mu\mathrm{as}$ and in $-15\mu\mathrm{as} \lesssim X \lesssim 15\mu\mathrm{as}$ are the teardrop-shaped component. The relatively less luminous part outside of them corresponds to the extended emission region in the counterjet. In the $Y = 50\ \mu\mathrm{as}$ slice and in the $Y = 200\ \mu\mathrm{as}$ slice, most of the radiation comes from the outflowing matter in the approaching jet. The asymmetry with respect to the Y-axis is due to the relativistic beaming effect, as we have mentioned above. The relativistic beaming effect also makes the intensity higher in the approaching jet ($Y > 0$) than in the counterjet ($Y < 0$). In the distant region from the BH (e.g., $Y = 200\ \mu\mathrm{as}$), this effect is more efficient due to the acceleration of the relativistic jets. The gravitational lensing also affects the images. The apparent jet width of the counterjet is wider than that of the approaching jet, i.e., one may find that the brighter emission regions are wider in the slices of $Y = -50\ \mu\mathrm{as}$ and $-200\ \mu\mathrm{as}$ than those of $Y = 50\ \mu\mathrm{as}$ and $-200\mu\mathrm{as}$, respectively. It should be noted that the small spikes at around $-15\ \mu\mathrm{as} \lessapprox X \lessapprox 7.5\ \mu\mathrm{as}$ in the $Y = 50\ \mu\mathrm{as}$ slice represent the contamination by the emission from the counterjet.

Here we show in detail the origin of the four bright rings and the bright teardrop-shaped component. Figure 3 displays the distribution of n_e and some trajectories of the ray. The trajectory for ring (a) (the red line) leads from the observer screen to the BH. The photons emitted at the bottom of the separation surface (the dotted circle) immediately go out of the jet region and reach the observer screen. On the other hand, the blue line indicates that photons emitted at the bottom of the separation surface pass through the region of the counterjet before reaching the screen. This is due to the gravitational lensing. As a result, a slightly larger ring than ring (a) appears on the screen. Thus, the bottom of the separation surface in the approaching jet, which is a single ring shape, creates two rings on the observer screen. We note that the image of ring (b) is almost identical to the photon ring (see Figure 1) because the ray passes through the region inside the photon shell (the gray lines in Figure 3), where the unstable circular orbit forming the photon ring exists. The bottom of the separation surface in the counterjet also produces two rings. The trajectory indicated by the orange line reaches the observer screen directly from the bottom of the separation surface. This corresponds to ring (d). Ring (c) is generated by photons, which are emitted at the bottom of the separation surface, then pass through the interior of the counterjet and reach the observer screen.

We also find that the trajectory indicated by the purple line clearly passes through the separation surface in the counterjet. Because of the large emissivity at the separation surface, the bright teardrop-shaped component appears at the lower part of the screen ($Y < 0$). Light rays passing through the separation surface also reach the upper part of the screen ($Y > 0$). However, this emission is weaker than the boosted component of the approaching jet, so the teardrop-shaped component does not appear. We note that the asymmetry of the teardrop-shaped bright region with respect to the Y-axis (shown in Figure 1) is due to the relativistic beaming effect from the toroidal component of the fluid velocity.

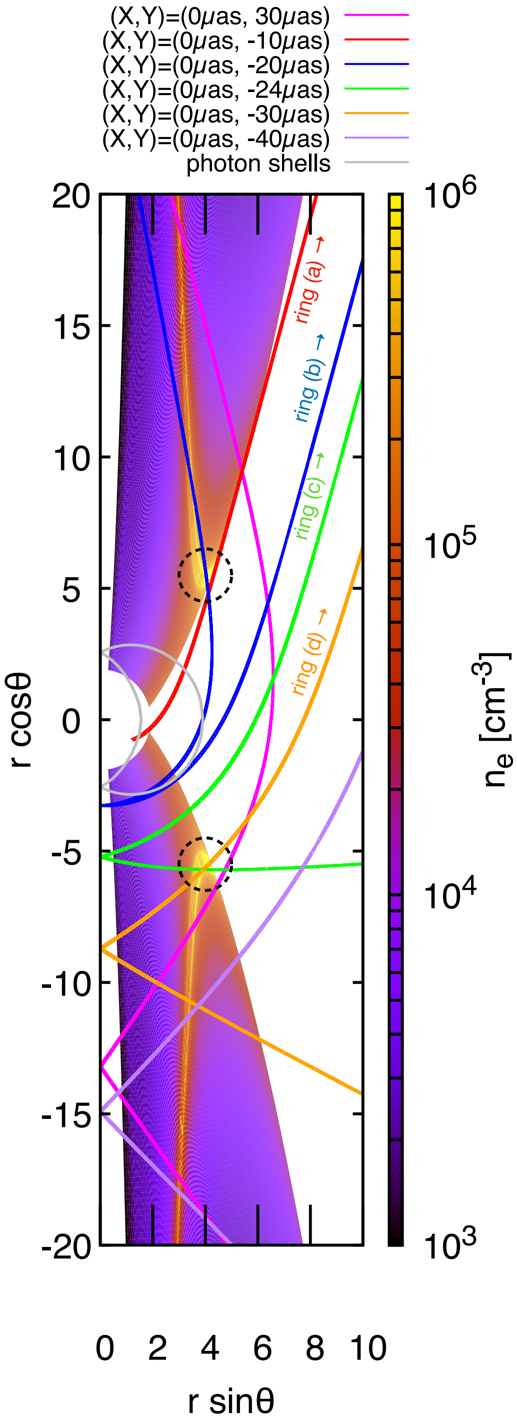

Figure 3. The two-dimensional color map of n_e. The trajectories of the ray that reaches rings (a), (b), (c), and (d) and $(X, Y) = (0\mu\mathrm{as}, -10\mu\mathrm{as})$, $(0\mu\mathrm{as}, -20\mu\mathrm{as})$, $(0\mu\mathrm{as}, -24\mu\mathrm{as})$, and $(0\mu\mathrm{as}, -30\mu\mathrm{as})$ on the observer screen are overlaid. We also show the other two trajectories that reach $(X, Y) = (0\mu\mathrm{as}, 30\mu\mathrm{as})$ and $(X, Y) = (0\mu\mathrm{as}, -40\mu\mathrm{as})$ on the observer screen, for reference. The black lines represent the separation surface. The gray lines are the photon shells (Teo 2003) and the black dotted circles point to the area on the bottom of the separation surface. The U-shape patterns near the jet axis are the printing artifacts.

3.2. Decomposing the Emission Structure

To decompose the emission structure of Figure 1, we show in Figure 4 the intensity maps of the emission originated from the four components: (i) the inflow component of the approaching jet; (ii) the outflow component of the approaching jet; (iii) the inflow component of the counterjet; and (iv) the outflow component of the counterjet.

The extended bright region in the second image from the left is originated from the outflow component in the approaching jet, which extends outward, starting from the separation surface. On

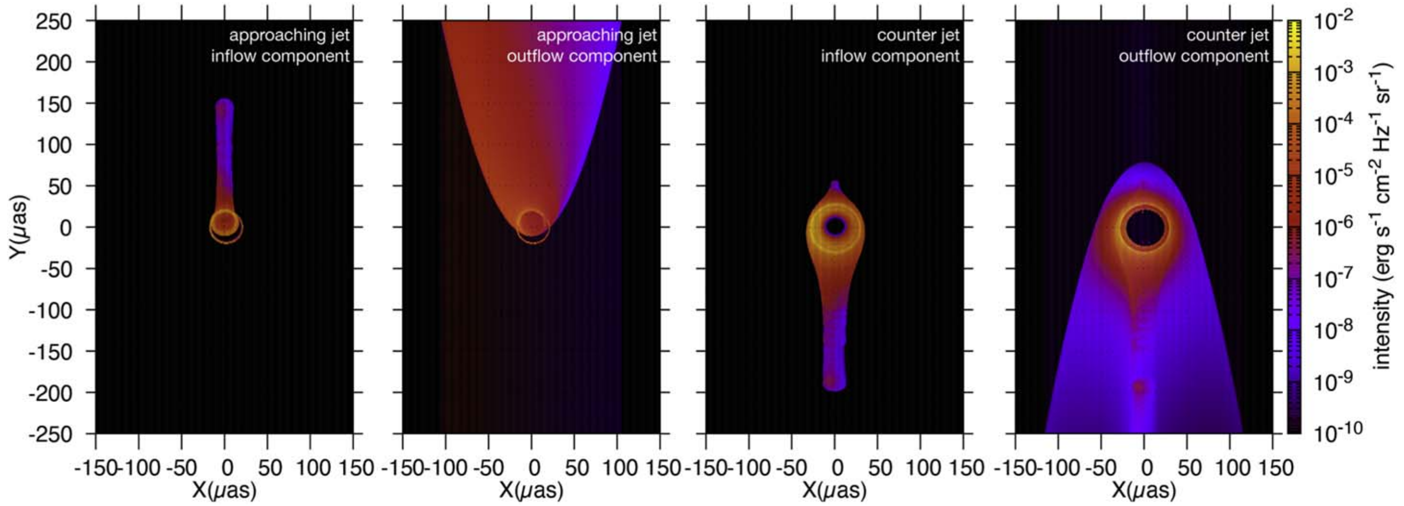

Figure 4. The intensity maps of the emission from the inflow component of the approaching jet, the outflow component of the approaching jet, the inflow component of the counterjet, and the outflow component of the counterjet, from the left to right panels. These are the decomposed intensity maps of the left panel of Figure 1. As in Figure 1, the several thin, ringlike red discontinuities around $Y \sim -100$ and -200 μas are the artifacts.

the other hand, the vertical structure in the leftmost image appears as a consequence of the emission from dense gas near the separation surface. The intensity in this vertical region is smaller than that in the extended region of the second image from the right and therefore does not appear in the approaching jet in Figure 1. The two bright rings in the two left-hand images are rings (a) and (b). The density (emissivity) in the region near the bottom of the separation surface is so large that the emission from this region forms bright rings. Since the fluid velocity in this region is positive on one side and negative on the other across the surface, the rings appear in both of the two left-hand panels. The extended emission region as well as the vertical region connects to ring (a). This means that ring (a) is the direct emission image of the separation surface. Conversely, ring (b) does not smoothly connect to other luminous regions because it is formed by photons that pass near the unstable orbit, which exists inside the photon shell (the gray lines depicted in Figure 3), and the indirect image is formed.

Two rings (c) and (d) appear in the two right-hand images. They are formed by radiation from the bottom of the separation surface in the counterjet. The extended region in the rightmost image is produced by the radiation from the outflow component of the counterjet, and the emission from the separation surface of the counterjet is responsible for the teardrop-shaped region in the second image from the right. The extended emission region is darkened by the relativistic beaming effect, so the teardrop-shaped region is visible in Figure 1. We note in the rightmost image that the extended region largely extends into the $Y > 0$ regime due to the gravitational lensing.

3.3. Parameter Dependencies

In this subsection, we change the viewing angle, observation frequency, BH spin, and energy distribution of the electrons, and compare the difference between the synthetic images.

3.3.1. Viewing Angle Dependence

Figure 5 shows the intensity maps and the optical depth maps when the viewing angle $\theta_{\rm view}$ is 5°, 45°, and 90°. As the viewing angle becomes larger, the broadly extended luminous region, which outlines the entire jet shape, becomes narrower. When $\theta_{\rm view} = 5^\circ$, the asymmetry with respect to the Y-axis is less significant compared to the other viewing angles. This is because the relativistic beaming via the toroidal velocity does not work so well. Conversely, when $\theta_{\rm view} = 90^\circ$, the relativistic beaming is most effective and the left side is brighter. The shape of the ring is closest to circular when $\theta_{\rm view} = 5^\circ$, and the shape is distorted as $\theta_{\rm view}$ approaches 90° because of the frame-dragging effect. The peak intensity and the peak optical depth also increase with $\theta_{\rm view}$. For the cases of $\theta_{\rm view} = 45^\circ$ and 90°, the peak positions of the intensity and the optical depth correspond to the bottom of the separation surface, where the toroidal component of the velocity is dominant, and the relativistic beaming effect enhances the intensity of the left side.

3.3.2. Frequency Dependence

The intensity maps and the optical depth map when the observational frequency is 86 GHz are shown in the top panels of Figure 6. Since the absorption opacity for the synchrotron increases with the decrease of the frequency, the optical depth is drastically enhanced and highly exceeds unity, especially in and around the photon ring and the ring images of the separation surfaces (see the top right panel). In the top middle panel, the rings are relatively faint, due to absorption by the optically thick medium against the synchrotron process. In the top left panel, we can see that the bright rings are blurred compared to the image at 230 GHz. The central bright area would correspond to the core of M87. The size of this bright region (diameter $\sim$60 μas) is roughly consistent with the recently observed 86 GHz ring image (Lu et al. 2023), whose diameter is $\sim$64μas.

The caveat is that the diameter of the ringlike image at 230 GHz is the same as that at 86 GHz in our model, while the EHT has not detected the 60 μas ringlike image. However, as roughly estimated below, this is expected to be solved if we construct the GRMHD jet model with the optical depth being thinner against synchrotron absorption (e.g., a lower-density GRMHD jet).

If the plasma is optically thin, the ratio of the radiative flux at 230 GHz to 86 GHz originated from the outermost brightest ring will be $F_\nu(\nu = 230\,{\rm GHz})/F_\nu\ (86\,{\rm GHz}) = (230\,{\rm GHz}/86\,{\rm GHz})^{(1-p)/2} \sim 0.29$. If $F_\nu(86\,{\rm GHz}) \sim 0.5$Jy, as observed

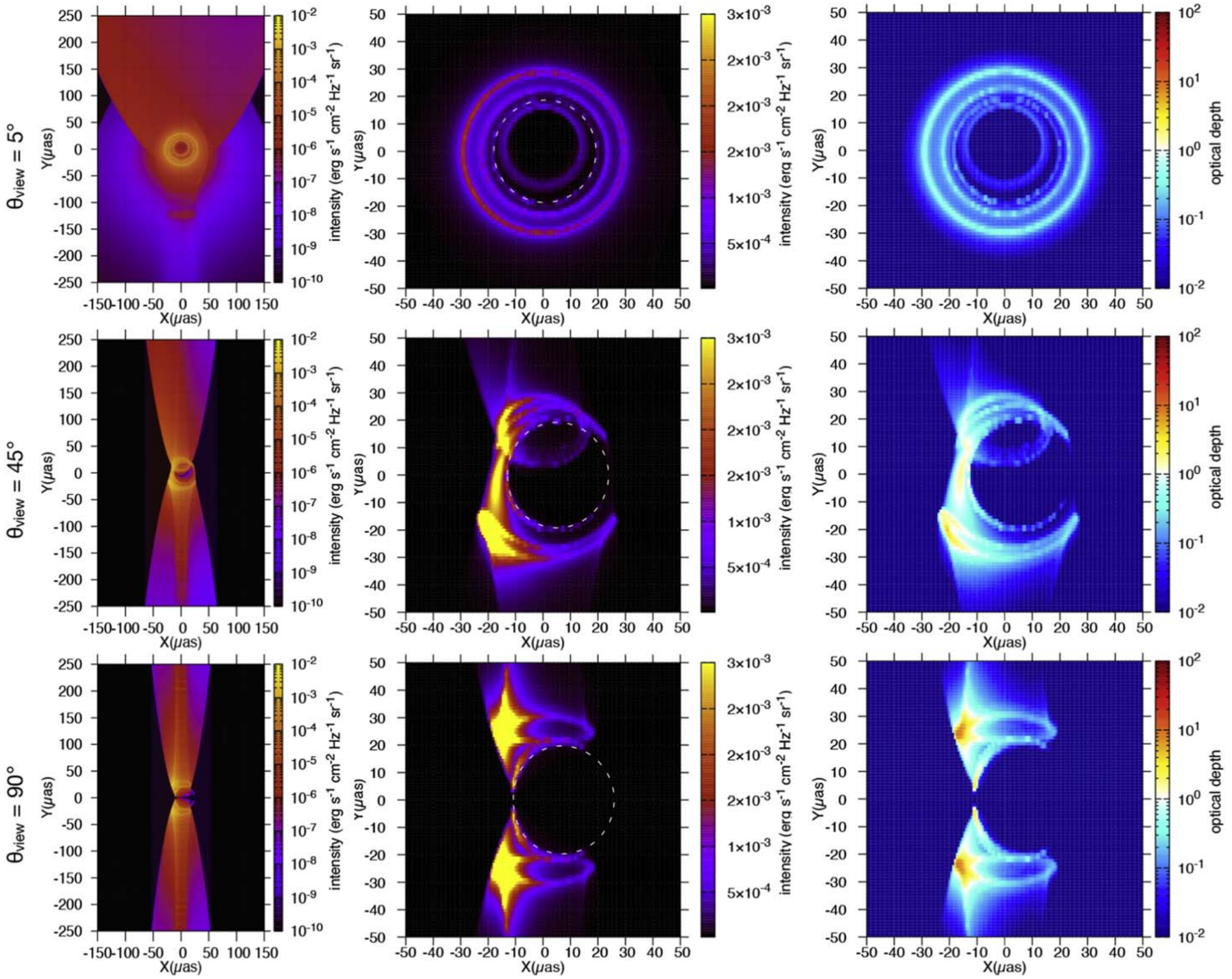

Figure 5. The intensity maps and the optical depth maps when the viewing angle $\theta_{\rm view}$ is 5° (top panels), 45°(middle panels), and 90° (bottom panels). The left panels are the log-scale intensity maps, the middle panels are the linear-scale intensity maps, and the right panels are the optical depth maps. The white dotted circles in the linear-scale intensity maps represent the location of the photon ring.

by GMVA, ALMA, and GLT (Lu et al. 2023), the radiative flux at 230 GHz is $F_\nu(230\,{\rm GHz}) \sim 0.15$Jy, which is ∼30% of that observed by EHT (Event Horizon Telescope Collaboration 2019a). Since the diameter of our ring (∼60 μas) is roughly 1.5 times larger than the EHT ring, the typical intensity of the outermost ring will be $\sim(1.0/1.5^2)\times 30\% \sim 10\%$, which is marginally lower than the detection limit of EHT due to its dynamical range. Therefore, the outermost ring can disappear in the current ability of the EHT consistently, if the plasma is set to be optically thin against the synchrotron absorption. This will be confirmed in future work. We note that the change of the model parameters of the GRMHD jet does not prominently affect the diameter of our outermost brightest ringlike images, since they are mainly regulated by the BH spin.

3.3.3. BH Spin Dependence

The middle and bottom panels of Figure 6 are the intensity and optical depth maps of the models, with the other BH spin parameter $a = 0.8$ and 0.95, respectively. The GRMHD models P2 ($a = 0.8$) and P3 ($a = 0.95$) in Ogihara et al. (2021) are here employed. The separation surface and the unstable photon orbit become closer to the BH as the spin parameter increases so that the sizes of the bright rings decrease. This ring size feature is consistent with the previous work using a toy model of the separation surfaces (Kawashima et al. 2021). The peak intensity and the optical depth are higher when the spin value is larger. Hence, small and clear rings appear in the case of $a = 0.95$. The structure of the extended emission region is not so sensitive to the spin parameter (see the left images).

3.3.4. Dependence on the Energy Distribution of the Electrons

Figure 7 shows the intensity slices when the power-law index of the electron energy distribution is $p = -1.1$ and -3.5 (fiducial). The intensity of the $p = -1.1$ model is larger than the $p = -3.5$ model in all the slices, due to the large number of high-energy photons present in the model of $p = -1.1$. The intensity contrast in the image becomes smaller when the energy distribution gets harder because the observable intensity

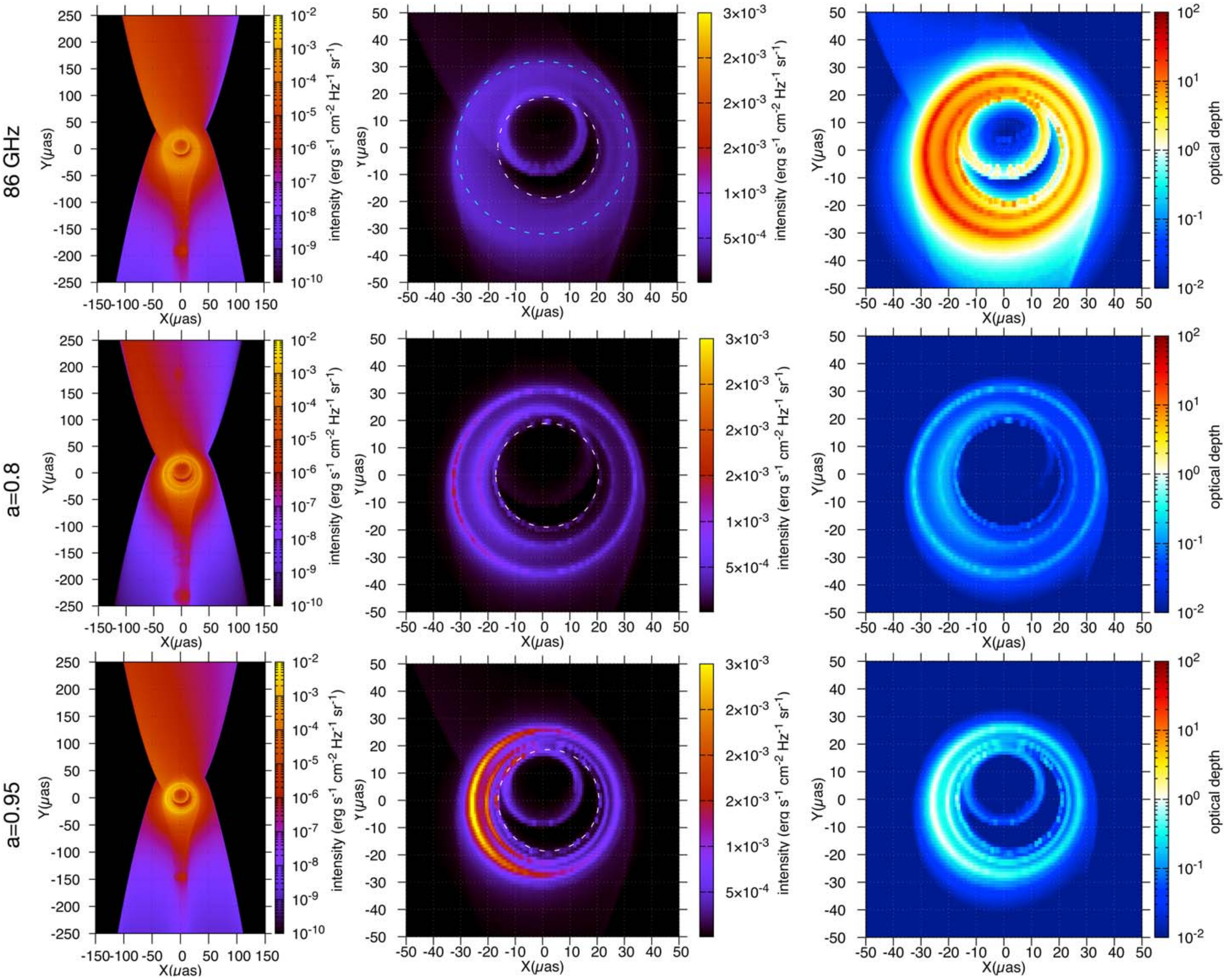

Figure 6. The intensity maps and optical depth maps when the observational frequency is 86 GHz (top panels), and when the BH spin parameter a is 0.8 (middle panels) and 0.95 (bottom panels), respectively. The left panels are the log-scale intensity maps, the middle panels are the linear-scale intensity maps, and the right panels are the optical depth maps. The white dotted circles in the linear-scale intensity maps represent the position of the photon ring. The diameter of the cyan dotted circle in the top middle panel is 64μas, which is almost as large as the ringlike images observed with GMVA, ALMA, and GLT at 86 GHz (Lu et al. 2023).

of the synchrotron photons emitted by the nonthermal electrons with the power-law index p is $I_\nu \propto \delta^{(5-p)/2}$, where $\delta = \nu/\nu'$ is the relativistic beaming factor, ν is the photon frequency measured by the observer, ν' is the photon frequency measured in the fluid rest frame, and I_ν is the specific intensity measured in the observer frame. The dependence of the observed intensity on δ is weaker when the power-law index is harder. In other words, the number density of the synchrotron-emitting electrons at the observing photon frequency becomes less different between the boosted area and the deboosted area when the energy distribution gets harder. The slope of the $Y = 200\,\mu$as slice is shallower in the $p = -1.1$ model than the $p = -3.5$ model, as well as the $Y = 50\,\mu$as slice, so that the above discussion can be confirmed.

Above, we mentioned the appearance of the weakly asymmetric intensity map with respect to $X = 0$ in the harder electron distribution model; the same discussion can be applicable to understanding the intensity asymmetry with respect to $Y = 0$ (i.e., the ratio of the approaching jet to the counterjet). The intensity ratio between the $Y = -200\,\mu$as slice and the $Y = 200\,\mu$as slice, and between the $Y = -50\,\mu$as slice and the $Y = 50\,\mu$as slice, is also smaller. For the $Y = 0$ slices, it should be noted that the ring components suffer the absorption efficiently and are in the optically thick regime when $p = -1.1$, which also contributes to the shallower contrast of the image.

4. Conclusions and Discussion

We have demonstrated the synthetic radio images inside a highly magnetized jet funnel based on the steady, axisymmetric, and semianalytic GRMHD models of Ogihara et al. (2021), where the plasma accelerates to the relativistic speed from the separation surface of the inflow and outflow. Here, the GRRT calculations, which take into account the synchrotron emission/absorption via the single-power-law nonthermal electrons, are performed using the `RAIKOU` code (Kawashima et al. 2023), assuming a vacuum outside the jets.

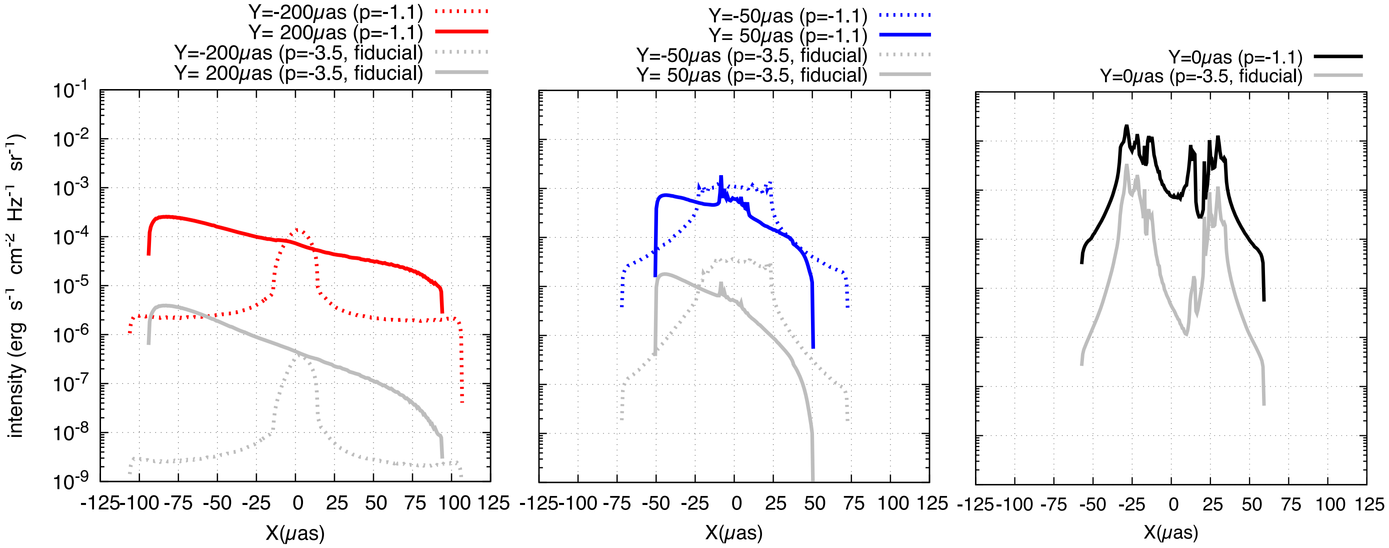

Figure 7. The intensity slices at ±200 μas (left panel), ±50 μas (middle panel), and 0 μas (right panel) of the image at 230 GHz when the power-law index of the electron energy distribution is $p = -1.1$ and -3.5. The gray lines are the slices of the $p = -3.5$ (fiducial) model and the colored lines are those of the $p = -1.1$ model.

For the case of $a = 0.9$, $\theta_{\mathrm{view}} = 15°$, and $p = -3.5$, the synthetic image at 230 GHz consists of the four bright rings, a bright teardrop-shaped structure extending downward from the rings, and the broadly extended components that outline the entire jet. The four rings are formed by the emission from the bottom of the separation surface, which is the strongest radiation source in our semianalytic GRMHD models. The plasma stagnates on and around the separation surfaces and the density of the plasma is high at the bottom of the separation surface near the jet funnel (see Figure 3 in Ogihara et al. 2021). All four rings are formed via the emission from the bottom of the separation surfaces in the approaching and counterjet regions. The ring with the smallest diameter is the direct image of the emission from the bottom of the separation surface in the approaching jet. The ring with the second smallest diameter is formed by the photons passing through the region near the unstable circular orbit around the BH, i.e., the trajectory is strongly bent by the gravity of the BH, after the emission from the bottom of the separation surface on the approaching jet side. The other two rings are the gravitationally lensed images of the emission from the bottom of the separation surface in the counterjet region.

The diameter of the brightest, outermost ring is approximately 1.5 times that of the photon ring diameter at 230 GHz. We discussed in Section 3.3.2 that this could be the origin of the ringlike feature observed by GMVA, ALMA, and GLT at 86 GHz (Lu et al. 2023), whose diameter is also ~1.5 times larger than that of the EHT ring image. Here, we discuss another possibility. It may also indicate that the BH mass is overestimated by about 1.5 times if the EHT captures this ring rather than the photon ring. In this case, the photon ring is hidden in the BH shadow. On the other hand, our result that the sizes of the bright rings at both 86 GHz and 230 GHz are nearly identical is inconsistent with the observations. It has been reported from the observations with GMVA, ALMA, and GLT that the ring diameter at 86 GHz is approximately $64^{+4}_{-8}\,\mu$as, which is about 1.5 times larger than the observed ring at 230 GHz. This contradiction may be caused by the disk radiation being ignored in the present work. If the disk radiation predominates over the separation surface radiation at 86 GHz, it could result in the appearance of a larger ring in the 86 GHz image than what is observed in this study. Here we note that due to the frequency dependence of the synchrotron opacity, the disk is likely to be brighter at 86 GHz than at 230 GHz.

The radiation from the separating surface in the counterjet other than from the bottom forms the teardrop-shaped structure. The outflow components in the approaching and counterjets are responsible for the broadly extended components. The relativistic beaming effect due to the toroidal velocity induces asymmetry about the Y-axis, and that due to the poloidal velocity produces asymmetry with respect to the X-axis.

The apparent jet width is narrower as θ_{view} approaches 90°. Then, the shape of the bright rings is distorted and part of the bottom of the separation surface is luminous, due to the relativistic beaming effect and the frame-dragging effect. It is also found that the ring signature becomes less distinct, because of the effective absorption when the observed wavelength is 86 GHz. We find that the rings tend to become smaller and clearer as the spin parameter increases. In addition, we find that when $p = -1.1$ is employed, the entire image becomes brighter and the difference between the brightness and darkness becomes smaller.

Although we only focus on the emission structure in $Y < 250\,\mu$as in this study, the observed limb-brightened features in the $Y \gtrsim (1\text{–}10)$ mas region would be explained by the force-free models (Ogihara et al. 2019; see also Takahashi et al. 2018). In the force-free models, a drift velocity is used as the fluid velocity, and the Lorentz factor increases linearly with the cylindrical radius. As the poloidal velocity increases, the toroidal component of the velocity decreases, which decreases the asymmetry of the jet image. In addition, the magnetic field and gas density are larger near the jet edge than around the axis. Thus, the limb-brightened structure is expected to appear.

In this study, we assumed that all the particles are nonthermal electrons and we used the single-power-law distribution for the electron energy spectrum in the entire jet region. However, the spectrum should be determined by particle acceleration and cooling, as well as by electron–positron pair creation. The pair creation by ambient photons originating from the surrounding disk or corona can produce ∼megaelectronvolt pairs (Kimura & Toma 2020). The distribution of the pairs has been studied by Mościbrodzka et al. (2011) and Wong et al. (2020). The combination with the inverse-Compton scattering may create higher-energy particles. The unscreened electric field parallel to the magnetic field accelerates plasma particles (so-called "gap acceleration"). The gap appears at the null-charge surface rather than the separation surface according to GR particle-in-cell simulations (Levinson & Cerutti 2018; Parfrey et al. 2019; Crinquand et al. 2020, 2021; Kisaka et al. 2020, 2022). Recently, it has been suggested that the injection of the charged particles inside the jet funnel can be realized via the cascades triggered by magnetic reconnection near the equatorial plane of the magnetically arrested disk in the vicinity of the BH (Kimura et al. 2022; Hakobyan et al. 2023), motivated by the recent GRMHD simulations with remarkably high spatial resolution (Ripperda et al. 2022). The change of the synthetic images depending on the difference in the electron energy distribution should be studied in future studies.

In this study, the density is high at the edge of the separation surface (as is also shown in Figure 3 of Ogihara et al. 2021), and the emission at that point contributes most of the brightness of the four rings. Therefore, the emission would weaken if the turbulence in the disk or wind occurs and the density at the edge decreases, although the detailed influence of the turbulence should be dealt with in another study.

The jet model used in this study is axisymmetric and does not include time variation. If a nonaxisymmetric structure is generated, the resulting images could be modified. In practice, time variabilities of gigaelectronvolt–teraelectronvolt gamma-rays are exhibited in M87 with a timescale of a day (e.g., Acciari et al. 2008) and in IC310 with several minutes (e.g., Aleksić et al. 2014). Incorporating time variability and nonaxisymmetric structure into the model, as well as including the emission and absorption via the accretion flow, to generate more realistic images is left for important future works.

Acknowledgments

We thank K. Toma for fruitful discussion. The numerical computations in this work were carried out at the Yukawa Institute Computer Facility. This work was supported by JSPS KAKENHI grant Nos. JP18K13594, JP23K03448, JP23H00117 (T.K.), JP18K03710, 21H01132, and JP21H04488 (K.O.). This work was also supported by "Program for Promoting Researches on the Supercomputer Fugaku" (Structure and Evolution of the Universe Unraveled by Fusion of Simulation and AI; grant No. JPMXP1020230406) and JICFuS.

ORCID iDs

Tomohisa Kawashima https://orcid.org/0000-0001-8527-0496
Ken Ohsuga https://orcid.org/0000-0002-2309-3639

References

Acciari, V. A., Beilicke, M., Blaylock, G., et al. 2008, ApJ, 679, 397
Aleksić, J., Ansoldi, S., Antonelli, L. A., et al. 2014, Sci, 346, 1080
Asada, K., & Nakamura, M. 2012, ApJL, 745, L28
Asada, K., Nakamura, M., & Pu, H.-Y. 2016, ApJ, 833, 56
Bekenstein, J. D., & Oron, E. 1978, PhRvD, 18, 1809
Blandford, R. D. 1976, MNRAS, 176, 465
Blandford, R. D., & Znajek, R. L. 1977, MNRAS, 179, 433
Boccardi, B., Krichbaum, T. P., Bach, U., Bremer, M., & Zensus, J. A. 2016, A&A, 588, L9
Boccardi, B, Perucho, M., Casadio, C., et al. 2021, A&A, 647, A67
Broderick, A. E., & Loeb, A. 2009, ApJ, 697, 1164
Bruni, G., Gómez, J. L., Vega-García, L., et al. 2021, A&A, 654, A27
Camenzind, M. 1986a, A&A, 156, 137
Camenzind, M. 1986b, A&A, 162, 32
Chael, A., Narayan, R., & Johnson, M. D. 2019, MNRAS, 486, 2873
Crinquand, B., Cerutti, B., Dubus, G., Parfrey, K., & Philippov, A. 2021, A&A, 650, A163
Crinquand, B., Cerutti, B., Philippov, A., Parfrey, K., & Dubus, G. 2020, PhRvL, 124, 145101
Cui, L., Lu, R.-S., Yu, W., et al. 2021, RAA, 21, 091
Cui, Y., Hada, K., Kawashima, T., et al. 2023, Natur, 621, 711
Davelaar, J., Olivares, H., Porth, O., et al. 2019, A&A, 632, A2
De Villiers, J.-P., Hawley, J. F., & Krolik, J. H. 2003, ApJ, 599, 1238
Dexter, J., Agol, E., & Fragile, P. C. 2009, ApJL, 703, L142
Dexter, J., McKinney, J. C., & Agol, E. 2012, MNRAS, 421, 1517
Doeleman, S., Blackburn, L., Dexter, J., et al. 2019, BAAS, 51, 256
Event Horizon Telescope Collaboration. 2019a, ApJL, 875, L1
Event Horizon Telescope Collaboration. 2019b, ApJL, 875, L2
Event Horizon Telescope Collaboration. 2019c, ApJL, 875, L3
Event Horizon Telescope Collaboration. 2019d, ApJL, 875, L4
Event Horizon Telescope Collaboration. 2019e, ApJL, 875, L5
Event Horizon Telescope Collaboration. 2019f, ApJL, 875, L6
Event Horizon Telescope Collaboration., Akiyama, K., Algaba, J. C., et al. 2021, ApJL, 910, L13
Giovannini, G., Savolainen, T., Orienti, M., et al. 2018, NatAs, 2, 472
Gold, R., McKinney, J. C., Johnson, M. D., & Doeleman, S. S. 2017, ApJ, 837, 180
Gracia, J., Vlahakis, N., Agudo, I., Tsinganos, K., & Bogovalov, S. V. 2009, ApJ, 695, 503
Hada, K., Doi, A., Kino, M., et al. 2011, Natur, 477, 185
Hada, K., Doi, A., Wajima, K., et al. 2018, ApJ, 860, 141
Hada, K., Kino, M., Doi, A., et al. 2016, ApJ, 817, 131
Hada, K., Park, J. H., Kino, M., et al. 2017, PASJ, 69, 71
Hakobyan, H., Ripperda, B., & Philippov, A. A. 2023, ApJL, 943, L29
Huang, L., Pan, Z., & Yu, C. 2019, ApJ, 880, 93
Huang, L., Pan, Z., & Yu, C. 2020, ApJ, 894, 45
Janssen, M., Falcke, H., Kadler, M., et al. 2021, NatAs, 5, 1017
Kawashima, T., Ohsuga, K., & Takahashi, H. R. 2023, ApJ, 949, 101
Kawashima, T., Toma, K., Kino, M., et al. 2021, ApJ, 909, 168
Kim, J. Y., Krichbaum, T. P., Lu, R. S., et al. 2018, A&A, 616, A188
Kimura, S. S., & Toma, K. 2020, ApJ, 905, 178
Kimura, S. S., Toma, K., Noda, H., & Hada, K. 2022, ApJL, 937, L34
Kino, M., Takahara, F., Hada, K., et al. 2015, ApJ, 803, 30
Kino, M., Takahara, F., Hada, K., & Doi, A. 2014, ApJ, 786, 5
Kisaka, S., Levinson, A., & Toma, K. 2020, ApJ, 902, 80
Kisaka, S., Levinson, A., Toma, K., & Niv, I. 2022, ApJ, 924, 28
Koide, S., Shibata, K., & Kudoh, T. 1998, ApJL, 495, L63
Kovalev, Y. Y., Lister, M. L., Homan, D. C., & Kellermann, K. I. 2007, ApJL, 668, L27
Kovalev, Y. Y., Pushkarev, A. B., Nokhrina, E. E., et al. 2020, MNRAS, 495, 3576
Levinson, A., & Cerutti, B. 2018, A&A, 616, A184
Lu, R.-S., Asada, K., Krichbaum, T. P., et al. 2023, Natur, 616, 686
McKinney, J. C., & Gammie, C. F. 2004, ApJ, 611, 977
Mertens, F., Lobanov, A. P., Walker, R. C., & Hardee, P. E. 2016, A&A, 595, A54
Mizuno, Y. 2022, Univ, 8, 85
Mizuno, Y., Nishikawa, K.-I., Koide, S., Hardee, P., & Fishman, G. J. 2006, arXiv:astro-ph/0609004
Mościbrodzka, M., Falcke, H., & Shiokawa, H. 2016, A&A, 586, A38
Mościbrodzka, M., Falcke, H., Shiokawa, H., & Gammie, C. F. 2014, A&A, 570, A7
Mościbrodzka, M., Gammie, C. F., Dolence, J. C., & Shiokawa, H. 2011, ApJ, 735, 9
Nagai, H., Haga, T., Giovannini, G., et al. 2014, ApJ, 785, 53
Nakahara, S., Doi, A., Murata, Y., et al. 2019, ApJ, 878, 61
Nakahara, S., Doi, A., Murata, Y., et al. 2020, AJ, 159, 14
Nakamura, M., Asada, K., Hada, K., et al. 2018, ApJ, 868, 146
Nathanail, A., & Contopoulos, I. 2014, ApJ, 788, 186
O' Riordan, M., Pe'er, A., & McKinney, J. C. 2018, ApJ, 853, 44
Ogihara, T., Ogawa, T., & Toma, K. 2021, ApJ, 911, 34

Ogihara, T., Takahashi, K., & Toma, K. 2019, ApJ, 877, 19
Orienti, M., D'Ammando, F., Giroletti, M., et al. 2020, MNRAS, 491, 858
Parfrey, K., Philippov, A., & Cerutti, B. 2019, PhRvL, 122, 035101
Park, J., Hada, K., Nakamura, M., et al. 2021, ApJ, 909, 76
Piner, B. G., Pant, N., & Edwards, P. G. 2010, ApJ, 723, 1150
Piner, B. G., Pant, N., Edwards, P. G., & Wiik, K. 2009, ApJL, 690, L31
Porth, O., Chatterjee, K., Narayan, R., et al. 2019, ApJS, 243, 26
Pu, H.-Y., Nakamura, M., Hirotani, K., et al. 2015, ApJ, 801, 56
Pu, H.-Y., & Takahashi, M. 2020, ApJ, 892, 37
Ripperda, B., Liska, M., Chatterjee, K., et al. 2022, ApJL, 924, L32
Takahashi, K., Toma, K., Kino, M., Nakamura, M., & Hada, K. 2018, ApJ, 868, 82
Takahashi, M., Nitta, S., Tatematsu, Y., & Tomimatsu, A. 1990, ApJ, 363, 206
Tanabe, K., & Nagataki, S. 2008, PhRvD, 78, 024004
Teo, E. 2003, GReGr, 35, 1909
Tseng, C.-Y., Asada, K., Nakamura, M., et al. 2016, ApJ, 833, 288
Tsunetoe, Y., Mineshige, S., Ohsuga, K., Kawashima, T., & Akiyama, K. 2020, PASJ, 72, 32
Walker, R. C., Hardee, P. E., Davies, F. B., Ly, C., & Junor, W. 2018, ApJ, 855, 128
Walker, R. C., Ly, C., Junor, W., & Hardee, P. J. 2008, JPhCS, 131, 012053
White, C. J., Stone, J. M., & Gammie, C. F. 2016, ApJS, 225, 22
Wong, G. N., Ryan, B. R., & Gammie, C. F. 2020, ApJ, 907, 73
Zakamska, N. L., Begelman, M. C., & Blandford, R. D. 2008, ApJ, 679, 990
Znajek, R. L. 1977, MNRAS, 179, 457